Heteroepitaxial Growth and Nucleation of Iron Oxide Films on Ru(0001)

Guido Ketteler[†] and Wolfgang Ranke*

Department of Inorganic Chemistry, Fritz-Haber-Institute of the Max-Planck Society, Faradayweg 4-6, 14195 Berlin, Germany

Heteroepitaxial growth of thin iron oxide films on Ru(0001) is investigated by scanning tunneling microscopy (STM) and low-energy electron diffraction (LEED). Metastable FeO(111) layers grow with a thickness up to 4 monolayers (ML) on Ru(0001) by oxidation of the corresponding amount Fe in 10^{-6} mbar O_2 at 870 K with a final anneal to 1000 K. Prolonged oxidation transforms the whole film to the thermodynamically more stable Fe_3O_4(111) phase. This phase transition requires at least two bulk repeat units of Fe_3O_4(111) and does therefore not occur in very thin FeO(111) films. Oxidation of 1−3 ML thick FeO(111) films lead to a heterogeneous nucleation of Fe_3O_4(111) islands, preferentially at step edges where due to iron oxide diffusion the required thickness can locally be established. Homogeneous nucleation of self-assembled, periodic Fe_3O_4(111) nanodomains embedded in an ultrathin FeO(111) occurs in ∼4 ML thick FeO(111) films. The driving force is an electrostatic and thermodynamic energy gain. The results are compared to the Stranski-Krastanov growth of iron oxides on Pt(111) [Weiss, W.; Ritter, M. *Phys. Rev. B* **1999,** *59,* 5201]. Differences in the growth behavior of iron oxides on Ru(0001) and Pt(111) are discussed in terms of the different affinity of the iron oxide film toward both metals, showing that the stabilization mechanism and growth mode for the same metal oxide phases depends strongly on the substrate.

1. Introduction

During the last years well-defined oxide model catalyst systems with defined composition and surface termination have become available.[1−9] The preparation of these model catalysts is crucial as their surface chemistry is strongly influenced by the chemical and electronic termination, atomic surface defects, surrounding gas atmosphere, etc.[10−22] Unfortunately, most metal oxides exhibit poor or no conductivity and the common electron-related characterization techniques such as electron spectroscopy and scanning tunneling microscopy (STM) cannot be applied. Therefore, thin oxide films grown on conducting substrates have gained much interest. Well-ordered oxide films can be obtained by oxidizing the surface region of metal single crystals[4,23,24] or by heteroepitaxial metal oxide growth. Such films have been prepared by molecular-beam epitaxy in oxygen atmosphere[25] or NO$_2$,[26,27] by oxygen-plasma assisted molecular-beam epitaxy,[14,28,29] or by metal deposition and subsequent oxidation.[8,21,30,31] All these techniques have some unique features which in some cases may lead to differing surface terminations or compositions (see for example ref 18), and in case of polar films, the surface region may differ from the surface region of single crystals due to the boundary condition at the interface.[13]

For metals and semiconductors, a detailed microscopic picture of epitaxial growth has developed in the past.[32−34] In general, heteroepitaxial growth is determined by the energy balance between the surface free energy of the substrate and the growing film and the interface energy which depends on the specific geometric (e.g., strain due to lattice misfit) and chemical (e.g., interfacial alloying) interaction of the interface layers.[35] In such studies, it has been recognized that growth may lead under certain conditions to highly ordered nanostructures of uniform size.[36] For example, Stranski-Krastanov growth of heterolayered systems is exploited to prepare highly uniform and regularly spaced semiconductor quantum dot arrays.[37−39] Reconstructions, prepatterned substrates, or thickness-dependent strain relief can lead to nanopatterned surfaces for metal on metal growth.[40−42] Due to the extraordinary properties of iron oxides, it would be highly interesting to realize such nanostructured systems on the basis of iron oxides. This would provide interesting new insights into the magnetism of spinel nanostructures and might become relevant for the realization of quantum magnetic disks.[43] Thin Fe_3O_4 films are also of high interest as a source for spin-polarized electrons in devices based on the giant magnetoresistance (GMR) effect.[44]

Due to the lower surface energy of most metal oxides, most metals grow in the form of three-dimensional clusters on these surfaces.[6,45] One exception is the recently realized growth of laminar Co films on a hydroxylated Al_2O_3(0001).[46] In this case, the strong interaction of the Co atoms with the hydroxylated oxide surface (i.e., the interface energy) determines the growth mode. On the other hand, growth studies of metal oxides on substrates are rare. This is due to the high complexity as stoichiometric conversion to another phase might occur[19] with associated changes of the surface free energy and interfacial energy. In the case of polar oxides, the stability of the growing film furthermore depends on the electrostatics of the system. For example, on Pt(111), iron oxides grow in a Stranski-Krastanov growth mode.[47,48] The growth is determined by the electrostatic surface free energy of the growing polar iron oxide film.[49] On many different substrates, including Pt(111), Pt(100), Cu(001), and α-Al_2O_3(0001), initially an ultrathin FeO(111) film forms during growth.[47−53] Vanadium oxide films grown on Pd(111) reveal a sequence of layer-dependent structures and oscillating oxidation states.[54−56] These metastable phases are interface-mediated and transform into stable, three-dimensional

* Corresponding author. E-mail: ranke@fhi-berlin.mpg.de.
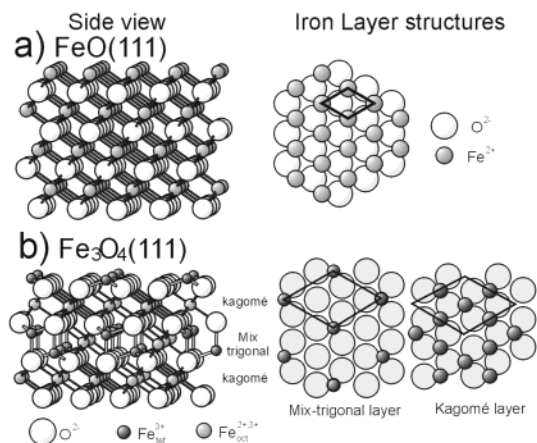† Also: FU Berlin, Fachbereich Biologie, Chemie, Pharmazie, Takustr. 3, 14195 Berlin, Germany.

Figure 1. (a) Slightly tilted side view and top view of FeO(111) including the two-dimensional unit cell. (b) Slightly tilted side view of Fe_3O_4(111) and top view of the iron sublayers of Fe_3O_4(111).

V_2O_3(0001) crystallites beyond a critical thickness of 3 monolayer equivalents. For oxide on oxide growth, the epitaxial growth mode is mainly determined by the interfacial energies arising from the lattice mismatch between the oxygen sublattices.[26,28,29,57]

Iron oxides are of high importance as catalyst materials for a number of different chemical reactions,[58] in particular the dehydrogenation of ethylbenzene to styrene.[59,60] Three thermodynamically stable iron oxide phases exist: $Fe_{1-x}O$ crystallizes in the cubic sodium chloride structure (a = 4.28...4.32 Å, depending on the iron content) (Figure 1a), ferrimagnetic Fe_3O_4 with an inverse spinel structure (cubic, a = 8.396 Å) (Figure 1b) and hexagonal α-Fe_2O_3 (a = 5.034 Å, c = 13.752 Å). The latter is the thermodynamically stable iron oxide phase for all oxygen pressures at room temperature. In general, the oxide stoichiometry is determined by the temperature and the oxygen gas pressure.[19] As epitaxial growth always takes place under nonequilibrium conditions, the oxidation kinetics is of high importance. For instance, the metal deposition rate is important for the oxide phase formation and their crystallographic quality.[29] In the case of thin iron oxide films, unique kinetically stabilized surface phases are formed at conditions close to a phase transition from one bulk phase to another and for ultrathin films.[19] Sometimes different iron oxide phases arrange in an ordered way ("biphase ordering").[61-64]

In this work, we have investigated the growth of iron oxides on Ru(0001). Fe films grown on Ru(0001) are of interest concerning ultrathin film magnetism[65,66] and as bimetallic catalysts for the ammonia and Fischer−Tropsch synthesis.[67-69] Different contributions to the growth mechanism are identified, specifically the influence of the amount Fe deposited, oxidation time, and substrate defect concentration on the growth morphology. On Ru(0001), the stronger affinity of iron and oxygen to the substrate stabilizes the oxide film in a different way than on Pt and leads to differences in the growth mechanism.

2. Experimental Section

The experiments were carried out in an ultrahigh vacuum chamber with a base pressure of 1×10^{-10} mbar which is described in detail elsewhere.[70] It is equipped with a scanning tunneling microscope (STM, Burleigh), a combined low-energy electron diffraction (LEED) and Auger electron spectroscopy (AES) optics, as well as oxygen and argon gas inlet valves and a sputter gun. STM measurements were performed in the constant current mode using electrochemically etched tungsten

tips cleaned in situ by electron bombardment. Iron was evaporated by resistively heating an iron wire wrapped around a tungsten filament.

The Ru(0001) crystal was cleaned by numerous cycles of argon sputtering (1 keV, 3−5 μA) and subsequent annealing to 1000 K in 10^{-6} mbar oxygen and finally to 1450 K without oxygen. This results in a well-ordered surface exhibiting a sharp (1 × 1)-Ru(0001) LEED pattern with no contamination signals detectable in AES. Most STM images showed the characteristic, very stable subsurface Ar-bubbles;[71] however, we found no significant influence on the nucleation and growth of iron oxide films in the vicinity of the strained substrate surface. Onto the clean Ru(0001) substrate, different amounts of iron were deposited and subsequently oxidized for a few minutes at 870 K in 10^{-6} mbar O_2 with a final flash to 1000 K in 10^{-6} mbar O_2. The obtained films were cooled in the oxygen atmosphere until 550 K where oxygen was pumped off. All films were clean as monitored by Auger electron spectroscopy.

The following definitions of one monolayer are used throughout this paper: FeO(111) consists of alternating iron and oxygen sublayers (see Figure 1a). We define one FeO(111) monolayer as one such Fe−O bilayer, irrespective of possible lattice constant relaxations. One monolayer of Fe corresponds to the respective amount to obtain one monolayer of FeO(111) after oxidation. At submonolayer FeO(111) coverages, the O/Ru(0001)−(2 × 2) LEED pattern can be seen which forms on the bare Ru(0001) areas under oxidative conditions (see Section 4.1, Figure 15). Since monolayer FeO(111) films completely wet the Ru(0001) substrate, the reduction of the O/Ru(0001)−(2 × 2) LEED pattern allows an estimation when the first FeO(111) monolayer is closed. Assuming that the evaporation conditions of the Fe evaporator are constant, the disappearance of the O/Ru(0001)−(2 × 2) pattern in combination with STM large scale images was used to calibrate the evaporator. In combination with AES, the thicknesses of thicker films can be estimated. However, depending on the oxidation time and temperature, significant amounts of iron can diffuse into the Ru substrate. Further, for FeO(111) films thicker than 2 ML local height differences may occur as indicated by occasionally occurring multiple layer steps in STM (see below). For these reasons, precise thickness determinations of specific terraces are delicate.

3. Results

3.1. Interaction of Fe with Ru(0001). Figure 2a shows a 1500×1500 Å^2 STM image of three Ru(0001) terraces after about 2 ML of iron are deposited at room temperature. The iron forms clusters which are statistically distributed on the terraces. No flat iron terraces are visible. The ruthenium substrate steps have not changed their morphology when compared to the uncovered surface. The background intensity in the Ru(0001) LEED pattern has increased and no additional spots are observed which shows that the crystalline order of the iron clusters is not very good.

After deposition of about 0.4 ML of iron at an elevated substrate temperature of 600 K, several flat iron terraces are obtained (Figure 2b). Also, second monolayers of iron have formed before the first one is closed. Step heights are ∼2 Å and terraces are 200−500 Å wide. The measured step height of 2 Å agrees with the distance between consecutive (111) or (110) layers in γ-Fe or α-Fe, respectively. In contrast to Fe deposition at room temperature, the substrate step structure has changed considerably and no straight step edges exist anymore. The crystalline order of the iron terraces is reflected by weak additional spots in the LEED pattern (Figure 2c). The weak
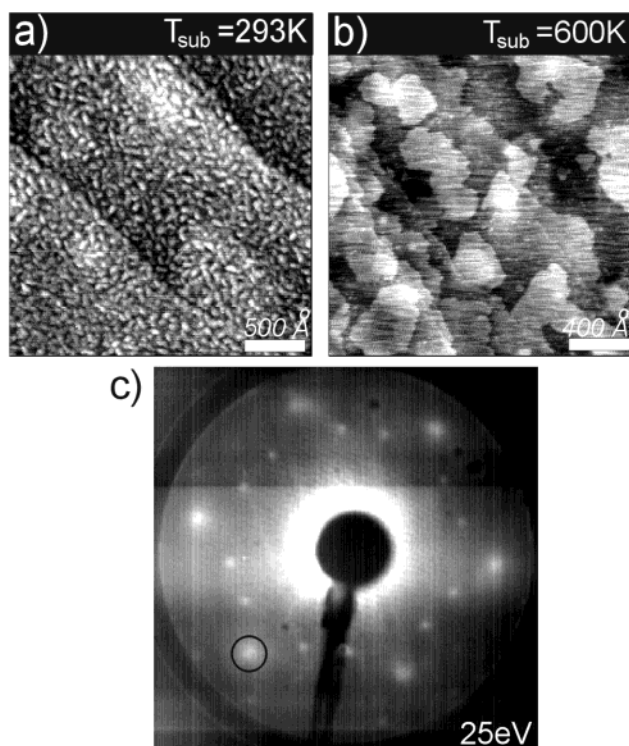
Figure 2. (a) 1500 × 1500 Å² STM image (I_t = 0.3 nA, U_B = +0.3 V) of ~2 ML Fe deposited at room temperature on Ru(0001). Fe forms clusters at this temperature. Two steps of the Ru(0001) substrate can be seen. (b) 2000 × 2000 Å² STM image (I_t = 0.5 nA, U_B = +0.3 V) of ~0.4 ML Fe deposited at 600 K on Ru(0001). Fe grows in layers at this temperature. (c) LEED image (25 eV) of the Fe layer of (b) on Ru(0001).

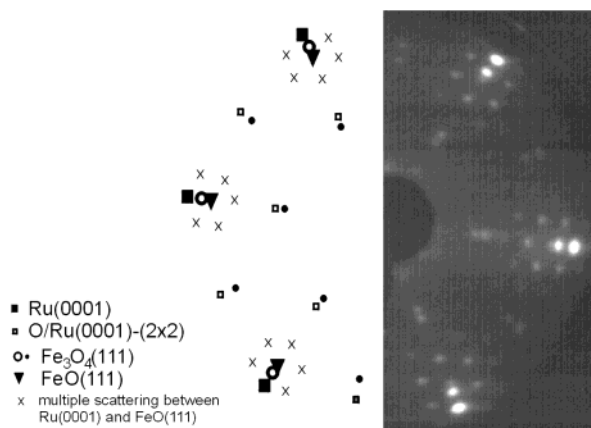**Figure 3.** Schematic LEED image (60 eV) of a mixed Fe_3O_4(111)/FeO(111)/Ru(0001) film showing the contributions of the different surface phases.

outer spots (e.g., the encircled spot in Figure 2c) are at the same positions as the O/Ru(0001)−(2 × 2) spots and may have formed due to adsorption of residual gas oxygen. Superimposed is a LEED pattern that corresponds to the c(4 × 2) oxygen phase of Fe films on Ru(0001) preannealed to 1030 K as shown by Egawa et al.[72] and will be discussed below.

3.2. Identification of Different Phases by Low-Energy Electron Diffraction (LEED). Depending on the deposited amount of Fe, different phases can be obtained after oxidation in 10^{-6} mbar O_2 which are characterized by their specific contributions to the LEED pattern. Figure 3 shows a LEED image taken from a film prepared by cumulative cycles of iron deposition and oxidation as shown in Figure 6e,f. The two iron oxide phases FeO(111) (Figure 1a) and Fe_3O_4(111) (Figure 1b),
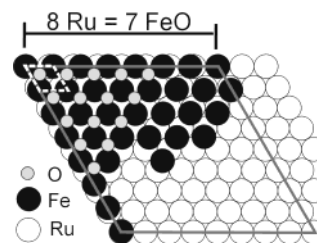

Figure 4. Schematic top view of one monolayer FeO(111) on Ru-(0001) with the so-called "7 on 8" coincidence structure.

and the O/Ru(0001)−(2 × 2) phase are present at the surface. The assignment of the spots is displayed in Figure 3. This demonstrates how the different phases can be identified from the LEED pattern.

The very bright, hexagonally arranged spots marked by a filled square in Figure 3 correspond to Ru(0001)−(1 × 1) spots. (2 × 2) spots (open square in Figure 3) from chemisorbed oxygen occur when uncovered parts of the Ru(0001) surface are exposed to O_2 (see Section 4.1). The circles mark the (1 × 1) LEED pattern from Fe_3O_4(111). The iron sublayers in Fe_3O_4-(111) form a (2 × 2) overlayer with respect to the closed packed oxygen layers in the spinel structure (see Figure 1b) resulting in a lattice constant of 5.94 Å (filled circles). The average O−O interatomic distance within one layer is 2.97 Å (open circles).

First-order diffraction spots of FeO(111) are located closer to the specular beam because of the larger unit cell compared to Fe_3O_4(111) (O−O distance within one layer of bulk FeO(111): 3.04 Å; filled triangles in Figure 3). These are surrounded by hexagonally arranged satellite spots (marked by an ×) which can be explained by multiple scattering between the FeO(111) film with the Ru(0001) substrate or in terms of diffraction at the large superstructure unit cell visible in the STM images (see Figure 11a−c). Both descriptions lead to the same satellite spot positions given by linear combinations of ruthenium substrate and FeO overlayer surface reciprocal lattice vectors. This pattern can be regarded as a Ru(0001)−(8 × 8) super-structure with unit cell vectors of 21.6 Å, and it results from coincidence of 7 FeO units with 8 Ru atoms ("7 on 8" structure, see Figure 4). Very similar LEED patterns were observed for ultrathin FeO(111) films on Pt(111).[49,50] There, four different Moiré superstructures characterized by different coincidence sites with the Pt(111) substrate were observed depending on the FeO(111) coverage in a range from 0 to 2.5 ML. Only beyond 2 ML FeO(111) coverage, unrotated (8 × 8) LEED patterns were obtained on Pt(111). LEED patterns from FeO(111) films with thicknesses between 0 and 4 ML on Ru(0001) are much sharper than those on Pt(111) and no elongations or spot splitting is observed. FeO(111) films on Ru(0001) also create significant intensities in second- and third-order multiple scattering events. The LEED patterns thus show that FeO(111) monolayer films grown on Ru(0001) are very well ordered and aligned with the Ru(0001) substrate.

The satellite LEED pattern resembles the LEED image shown by Egawa et al. for Fe films on Ru(0001) for coverages beyond 1 ML.[73] These authors reported a (6√3 × 6√3) R30° LEED pattern. It corresponds to a "6 on 9" coincidence structure rotated by 30° with respect to the "6 on 8" and "7 on 8" structures from FeO(111) films on Ru(0001). This leads to a different lattice constant of 4.05 Å (lattice constant of bcc Fe(110): 4.05 Å × 2.87 Å). The high structural similarity suggests that the first layer of our FeO-films are iron-terminated at the interface to the substrate with different coincidence structures due to differences in the lattice constants of the FeO vs Fe film.
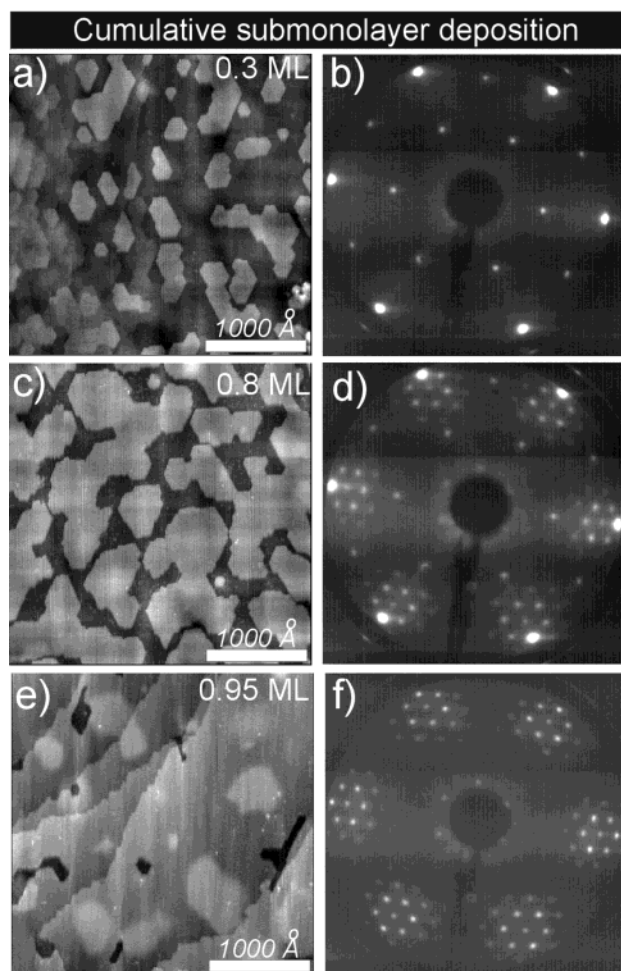
Heteroepitaxial Growth of Iron Oxide Films on Ru

J. Phys. Chem. B, Vol. 107, No. 18, 2003 **4323**

Figure 5. Consecutive growth stages of iron oxides by cumulative submonolayer deposition. (a) 3000 × 3000 Å^2 STM image ($I_t = 0.3$ nA, $U_B = +0.5$ V) and (b) LEED image (60 eV) of 0.3 ML FeO(111); (c) 3000 × 3000 Å^2 STM image ($I_t = 0.5$ nA, $U_B = +0.5$ V) and (d) LEED image (60 eV) of 0.8 ML FeO(111); (e) 3000 × 3000 Å^2 STM image ($I_t = 0.5$ nA, $U_B = +0.8$ V) and (f) LEED image (60 eV) of 0.95 ML FeO(111).

Figure 6. Consecutive growth stages of iron oxides beyond 1 ML coverage by cumulative deposition leading to Fe$_3$O$_4$ islands beyond 1.5 ML. (a) 3000 × 3000 Å^2 STM image ($I_t = 0.5$ nA, $U_B = +0.9$ V) and (b) LEED image (60 eV) of 1.2 ML FeO(111). (c) 3000 × 3000 Å^2 STM image ($I_t = 1.0$ nA, $U_B = +0.75$ V) and (d) LEED image (60 eV). (e) 5000 × 5000 Å^2 STM image ($I_t = 0.5$ nA, $U_B = +0.8$ V) and (f) LEED image (60 eV).

3.3. Growth of Iron Oxides on Ru(0001) by Cumulative Fe Deposition. Figure 5 shows STM images and LEED patterns of consecutive stages of the cumulative iron oxide growth below 1 ML. After deposition of about 0.3 ML Fe and oxidation in 10^{-6} mbar oxygen, hexagonally shaped first layer islands with a height of one Fe−O bilayer are formed (Figure 5a). With increasing coverage, these islands grow laterally and some of them coalesce (Figure 5c). No second layer islands form before the first monolayer FeO(111) is completed. Finally, the film wets the Ru(0001) substrate completely.

The LEED pattern changes in a characteristic manner: First, the O/Ru(0001)−(2 × 2) pattern dominates although already about 30% of the surface is covered by the oxide film (Figure 5b). The Ru(0001) spots are very bright at this energy and intense FeO(111) spots develop only beyond ∼0.5 ML (Figure 5d). When approaching monolayer coverage, the O/Ru(0001)−(2 × 2) pattern gets weaker and the FeO(111) satellite pattern with a lattice constant of 3.08 Å dominates. The FeO(111) lattice constant is 3.08 Å ("7 on 8" structure). Upon completion of the first monolayer, the O/Ru(0001)−(2 × 2) pattern vanishes (Figure 5f).

Figure 6 shows cumulative growth stages beyond 1 ML coverage. First, a second monolayer FeO(111) develops (Figure 6a,b), before hexagonally shaped islands with a height of ∼20
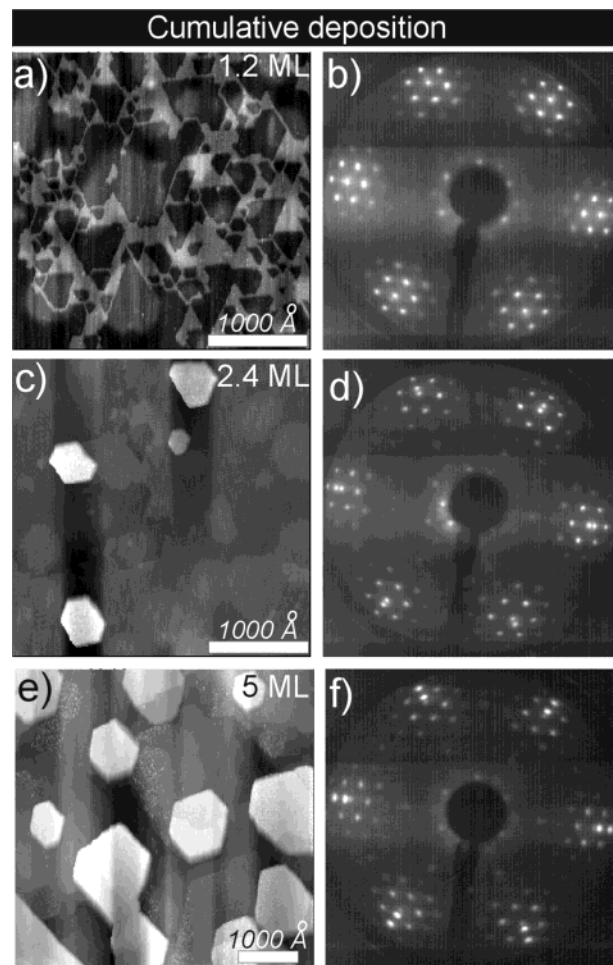
Å start to nucleate (Figure 6c). The LEED pattern now shows additional spots from Fe$_3$O$_4$(111) (Figure 6d) identifying the islands as Fe$_3$O$_4$. Upon repeated cycles of iron deposition and oxidation, these islands grow in number and size (Figure 6e). As the Fe$_3$O$_4$(111) islands grow, the LEED pattern shows most intense spots for Fe$_3$O$_4$(111), but surprisingly also the Ru(0001)−(1 × 1) spots gain intensity and weak O/Ru(0001)−(2 × 2) spots develop (Figure 6f). This shows that although the islands grow, the FeO(111) monolayer film coverage between the islands decreases upon repeated cycles of iron deposition and subsequent oxidation. This behavior will be discussed in more detail below (Sections 3.5 and 4.5).

3.4. Growth of 1−4 ML FeO(111) by One-Turn Fe-Deposition. To obtain closed Fe$_3$O$_4$(111) films, many cycles of iron deposition and oxidation have to be repeated. This procedure may be shortened when larger amounts of iron are deposited in each deposition cycle. Figure 7 shows LEED patterns and Auger spectra of FeO(111) films after deposition and oxidation of 1−3 ML Fe deposited in one turn. For coverages from 1 to 4 ML LEED shows the characteristic FeO(111) satellite pattern. Compared to a 1 ML thick film (Figure 5f), the satellite spots get weaker with increasing coverage while the FeO(10) main diffraction spots increase in intensity. STM shows flat terraces with well-ordered long-range Moiré modula-
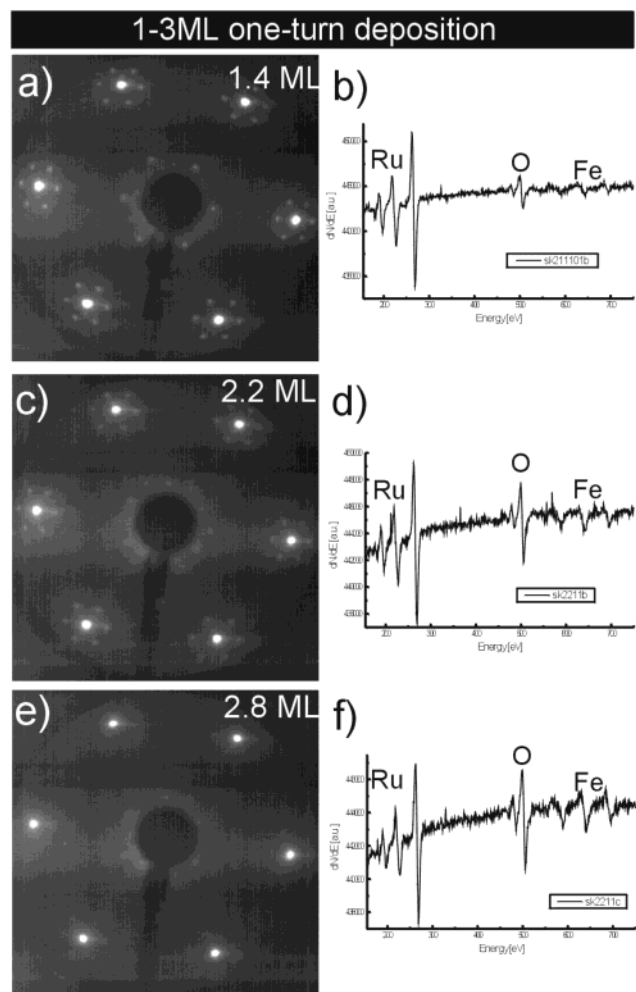
Figure 7. LEED patterns (60 eV) and Auger spectra of thicker FeO-(111) films obtained by one-turn deposition. (a,b) 1.4 ML; (c,d) 2.2 ML; (e,f) 2.8 ML.

tions (see Figure 12), therefore the weak satellite LEED spots are very likely caused by multiple diffraction at the Ru/FeO interface. As no O/Ru(0001)−(2 × 2) LEED spots occur, also these films are closed. Nevertheless, for all coverages the LEED pattern is quite sharp with low background intensity indicating good crystalline order. FeO(111) films with a thickness of ∼1 ML are very flat and closed within the range accessible by STM (i.e., over several micrometers). For thicker films, sometimes step edges which are multiples of 2.5 Å high are observed indicating that it would be more appropriate to describe these films as very extended flat crystallites (several 1000 Å, see for example Figure 8a) with local height differences. Sometimes extended Moiré FeO(111) terraces coexist with first nucleating Fe₃O₄(111) islands (e.g., marked by an arrow in Figure 8b).

3.5. Annealing of 2−4 ML Thick FeO(111) Films. Annealing of FeO(111) films with thicknesses beyond 1 ML leads to the nucleation of small Fe₃O₄(111) islands, initially at step edges of the FeO(111) film (Figure 9a). Upon prolonged oxidation, these islands grow in size and number (Figure 9c,e). Simultaneously, the LEED pattern changes in a characteristic manner. Upon prolonged annealing, the satellite spots gain intensity and additionally faint Fe₃O₄(111) spots appear. Finally, the O/Ru(0001)−(2 × 2) pattern reappears and gains intensity while the FeO(111) satellite pattern gets progressively weaker (Figure 9f). As no iron is deposited during this process, the growth of the Fe₃O₄(111) islands can only be explained by
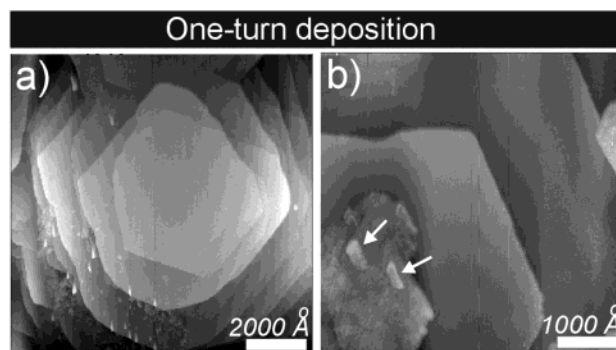

Figure 8. (a) 1 × 1 μm² STM image (I_t = 1.0 nA, U_B = +0.15 V) of more than 4 ML FeO(111) after extended annealing at 1000 K in 10⁻⁶ mbar O₂ and flashing to 1170 K. (b) 5000 × 5000 Å² STM image (I_t = 0.3 nA, U_B = +1.0V) of ∼4 ML thick FeO(111)/Ru(0001). The arrows indicate two nucleating Fe₃O₄(111) islands.

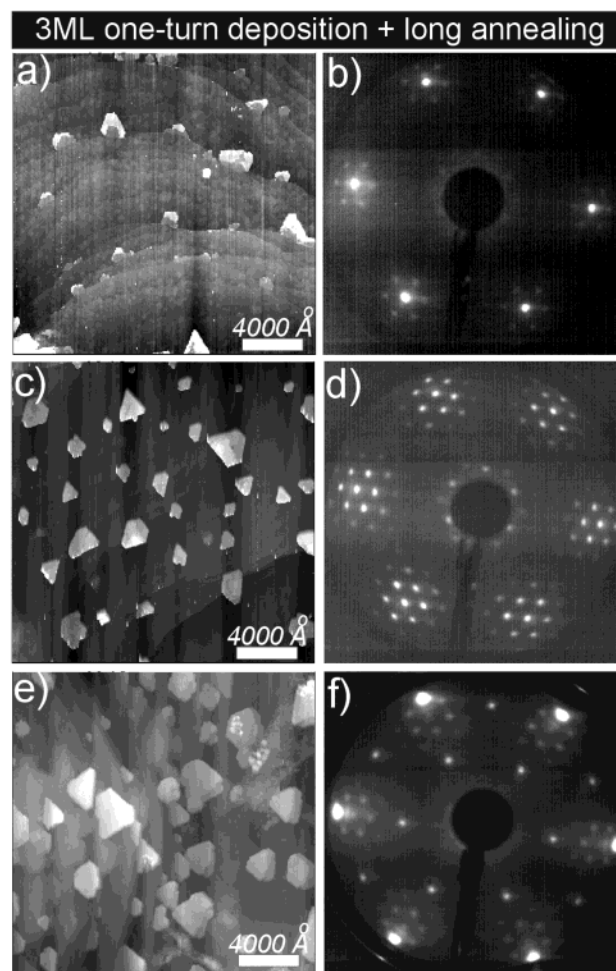**Figure 9.** Morphology changes during prolonged oxidation of a ∼3 ML thick FeO(111) film. (a) 2 × 2 μm² STM image (I_t = 0.7 nA, U_B = +0.5 V) of Fe₃O₄(111) islands nucleating at step edges. (b) The LEED pattern (60 eV) is dominated by FeO(111) spots. (c) 2 × 2 μm² STM image (I_t = 0.5 nA, U_B = +1.0 V). The Fe₃O₄(111) islands grow in size and number. (d) The LEED pattern (60 eV) shows intense satellite spots indicating ∼1 ML FeO(111) and additionally weak Fe₃O₄-(111) spots. (e) 2 × 2 μm² STM image (I_t = 1.0 nA, U_B = +0.1 V). Many large Fe₃O₄(111) islands have formed. (f) The LEED pattern (60 eV) shows contributions from Fe₃O₄(111), FeO(111), and O/Ru-(0001)−(2 × 2) showing that the FeO(111) thickness has decreased below 1 ML.

"eating up" the surrounding FeO(111) film. This is evident in the changes of the LEED pattern showing that the ∼3 ML thick
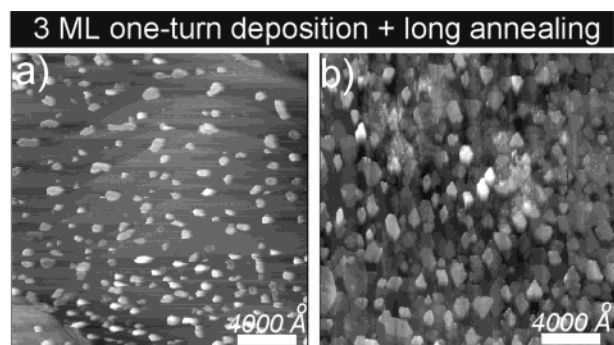
Heteroepitaxial Growth of Iron Oxide Films on Ru

J. Phys. Chem. B, Vol. 107, No. 18, 2003 **4325**

Figure 10. (a) $2 \times 2 \ \mu m^2$ STM image ($I_t = 0.5$ nA, $U_B = +0.5$ V) of nucleating $Fe_3O_4(111)$ islands on a Ru(0001) substrate with a high step density resulting in a high islands density nucleating at step edges. (b) $2 \times 2 \ \mu m^2$ STM image ($I_t = 0.5$ nA, $U_B = +0.8$ V) after further oxidation for 5 min even more islands have formed.

FeO(111) film in Figure 9b finally transforms to a submonolayer FeO(111) film in between the $Fe_3O_4(111)$ islands.

The nucleation of $Fe_3O_4(111)$ islands starts at step edges as can be seen in Figure 9a and also in Figure 10. Sometimes, the Ru(0001) substrate exhibits different step densities after sputter−annealing cycles. Figure 10 shows an FeO(111) film grown on a Ru(0001) surface with a high step density. Upon oxidation, the $Fe_3O_4(111)$ island density is much higher (Figure 10b). This shows the influence of the steps to the nucleation mechanism of $Fe_3O_4(111)$.

3.6. Defect Structures of Submonolayer FeO(111) Films. The FeO(111) overlayers can be characterized by their Moiré patterns in STM images (Figure 11) with a superstructure periodicity of 21.6 Å. For 1 ML thick films, the superstructure is extraordinarily well-ordered and perfectly aligned with the Ru(0001) substrate (Figure 11a−c). The lattice constant of films below 2 ML is 3.08 Å (Figure 11b) and results from coincidence of 7 FeO with 8 Ru atoms ("7 on 8" coincidence structure). A registry shift of the Moiré periodicity is observed when going from the lower to the higher terrace. Step edges are perfectly aligned with the Moiré periodicity and are completely different from the rounded shape of Ru(0001) step edges, showing that the growth of FeO(111) changes the substrate morphology. The step height is ∼2.1 Å which agrees with the Ru−Ru interlayer distance (bulk Ru(0001): 2.14 Å, bulk FeO(111): 2.5 Å).

Below 1 ML coverage, different kinds of defects can be seen (Figure 11d−g). For coverages below 0.1 ML, the Moiré superlattice is cut by several triangular trenches (Figure 11d). In most cases, these trenches surround one Moiré feature, sometimes three or more (bottom of Figure 11d). The triangular arrangement of these trenches is distorted and they are not aligned along crystallographic directions of the FeO(111) film or the Ru(0001) substrate. These trenches lead to a very limited long-range order of the Moiré pattern for FeO(111) films below 0.5 ML which causes the nonexisting or very weak satellite spots in the LEED pattern for these coverages (see Figure 5b). Approaching a coverage of one monolayer, the side lengths of these nearly triangularly arranged trenches increases and more extended FeO(111) Moiré regions are enclosed by them (Figure 11e). Still they are not aligned to the Moiré pattern and even cross single Moiré features. The closer the film approaches a full monolayer, these trenches grow in length and an extended long-range order of the Moiré pattern is established. Only occasionally long trenches are cutting through the film (Figure 11f). More localized defects can be seen now that appear as dark patches in the FeO(111) Moiré superlattice which may be
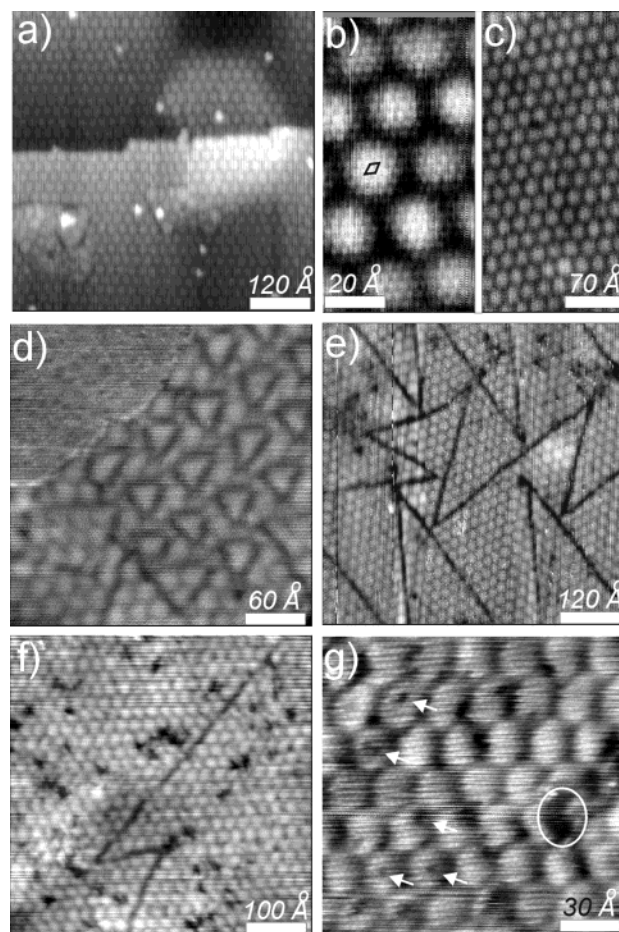

Figure 11. (a) 600×600 Å² STM image ($I_t = 0.2$ nA, $U_B = +0.8$ V) of the long-range ordered Moiré pattern forming on FeO(111) monolayer films. Step edges and the Moiré pattern are aligned. Steps have changed with respect to the clean Ru substrate (compare, e.g., with step edges in Figure 3a). (b) 50×100 Å² atomic resolution STM image ($I_t = 0.35$ nA, $U_B = -0.1$ V) of FeO(111) monolayer films. The lattice constant is 3.08 Å. (c) 165×350 Å² STM image ($I_t = 0.3$ nA, $U_B = +0.2$ V) of the Moiré pattern forming on FeO(111) monolayer films. (d) 300×300 Å² STM image ($I_t = 0.7$ nA, $U_B = +0.8$ V) of ∼0.1 ML FeO(111) growing at Ru(0001) steps. (e) 600×600 Å² STM image ($I_t = 1.0$ nA, $U_B = +0.3$ V) of nearly 1 ML FeO(111). (f) 500×500 Å² STM image ($I_t = 0.3$ nA, $U_B = +0.8$ V) of 0.95 ML FeO(111). (g) 150×150 Å² STM image ($I_t = 0.6$ nA, $U_B = +0.6$ V) showing atomic defects (marked by arrows) and extended defect regions (encircled). These can also be seen in (f) as dark areas in the Moiré pattern.

vacancy islands. In addition to the trenches, point defects of atomar dimensions can be seen in STM images of submonolayer coverages (marked by arrows in Figure 11g).

In summary, three different types of defects are present on submonolayer FeO(111) films: nearly triangularly arranged trenches cutting through the Moiré pattern, dark patches in the Moiré pattern, and atomic vacancies. Nearly all defects vanish when the first monolayer is closed, causing an extraordinarily sharp and intense LEED pattern.

3.7. Structures of 1−3 ML Thick FeO(111) Films Obtained by One-Turn Deposition. Large-scale STM structures of FeO(111) films with thicknesses between 1 and 3 ML are shown in Figures 12 and 13. In most cases, the 21.6 Å Moiré periodicity aligned to the atomic rows of the substrate is observed for all FeO(111) films with thicknesses below 4 ML. Occasionally, a Moiré pattern with a $\sqrt{3} \times \sqrt{3}$R30° periodicity of 37.4 Å with respect to the aligned 21.6 Å Moiré forms upon oxidation (Figure 12b) and sometimes vanishes when the film
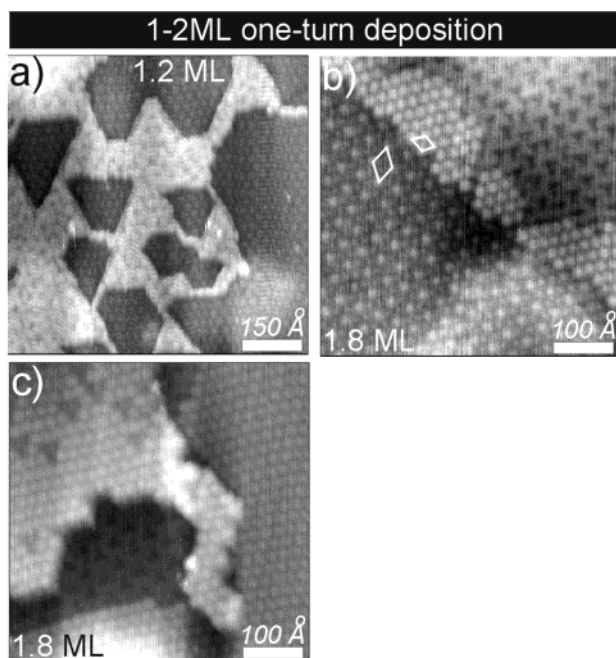
Figure 12. (a) 750 × 750 Å^2 STM image (I_t = 0.5 nA, U_B = +0.6 V) of 1.2 ML FeO(111). (b) 500 × 500 Å^2 STM image (I_t = 0.5 nA, U_B = +0.4 V) of ∼1.8 ML FeO(111) showing two different coexisting Moiré periodicities of 21.6 Å and $\sqrt{3}$ × 21.6 Å = 37.4 Å, rotated by 30°. Both superstructure unit cells are indicated by diamonds.

is oxidized slightly longer. It could not be attributed to a certain film thickness. In both cases, films are perfectly aligned with the substrate.

A thicker FeO(111) film is shown in Figure 13. Two different kind of steps appear forming kinks with 120° angles and 60° angles, respectively. The latter kind has a lower kink density (Figure 13a) and separates terraces with different Moiré patterns. Due to similarities with the structure of the second monolayer FeO(111) films grown on Pt(111)[49] and in agreement with the deposited amount of Fe, we attribute the lower terrace to the second FeO(111) layer while the upper terrace corresponds to the third layer. A change of the lattice constant from 3.08 to 3.58 Å occurs when going from the second to the third FeO(111) layer (Figure 13 d,e). The structure changes from a "7 on 8" coincidence structure to a "6 on 8" coincidence structure where 7 or 6 FeO units, respectively, coincide with 8 Ru units. The Moiré periodicity in both cases is the same (21.6 Å) and protrusions on both terraces are perfectly aligned with the Ru(0001) substrate. Further, bright lines form triangles on the lower 2 ML terrace (Figure 13b,c). These lines connect 2−6 Moiré features and have a width corresponding to one atomic feature but atomic features along these lines could not be resolved. These lines represent antiphase Moiré domain boundaries (see Figure 13 b,c). We were not able to control the number and size of these triangles systematically.

3.8. Self-Assembled Fe$_3$O$_4$(111) Nanostructures in ∼4 ML Thick FeO(111) Films. A film with a thickness of about 4 monolayers FeO(111) deposited in one evaporation−oxidation cycle is shown in Figure 14. When this thickness is reached, Fe$_3$O$_4$(111) nanodomains start to nucleate in an ordered fashion embedded in the FeO(111) film matrix.[64] This superstructure resembles the "biphase ordering" phenomenon on Fe$_3$O$_4$(111) and α-Fe$_2$O$_3$(0001).[62,63] The LEED pattern is dominated by FeO(111) spots and the Fe$_3$O$_4$(111) pattern is very weak. The lattice constant of the Fe$_3$O$_4$(111) nanodomains is strongly expanded to ∼7 Å (bulk value: 6 Å). These domains differ in size and shape but they form always at crossing points of the
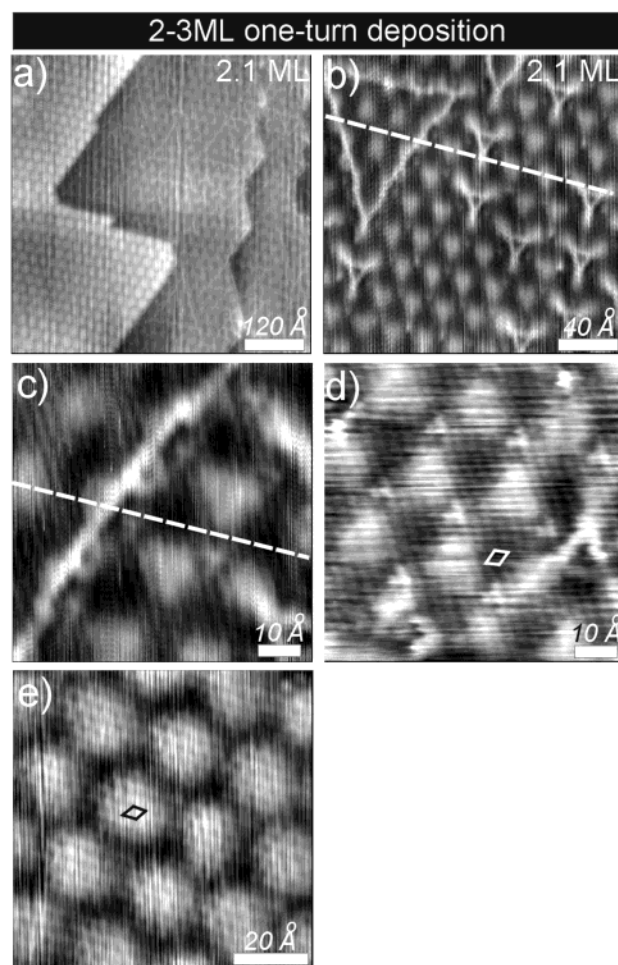

Figure 13. (a) 600 × 600 Å^2 STM image (I_t = 0.2 nA, U_B = +0.45 V) of ∼2.1 ML FeO(111). (b) 200 × 200 Å^2 STM image (I_t = 0.2 nA, U_B = +0.45 V) showing bright triangular lines. The inserted lines indicate the antiphase relationship across these features. (c) 70 × 70 Å^2 (I_t = 0.2 nA, U_B = +0.5 V) STM image of the second monolayer with one of the bright lines shown in (b). The inserted lines indicate the antiphase relationship across these features. (d) 70 × 70 Å^2 (I_t = 0.2 nA, U_B = +0.45 V) and (e) 80 × 80 Å^2 (I_t = 0.2 nA, U_B = +0.7 V) atomic resolution STM images of the second and third FeO(111) monolayer, respectively.

dark lines in the underlying FeO Moiré pattern. This results in a pseudohexagonal 50 Å × 65 Å superstructure. Also more extended Fe$_3$O$_4$(111) regions can be seen (right side of Figure 14a) as well as regions where no such domains are observed. For tunneling conditions as shown in Figure 14a, we were only able to resolve atomic protrusions on these regions and not on the FeO(111) Moiré patches which is due to the different electronic structure of both regions. The different chemical and electronic nature becomes evident after several hours of tunneling, when the Fe$_3$O$_4$(111) domains get covered by adsorbates (Figure 14b,c) while FeO(111) regions remain adsorbate-free. As no other elements than Fe, O, Ru can be detected by AES, these adsorbates correspond presumably to water from the residual gas. Such features have been previously observed on biphase ordered Fe$_3$O$_4$(111),[74] and X-ray and ultraviolet photoelectron spectroscopy (XPS, UPS) showed that dissociative H$_2$O chemisorption takes place on iron-terminated Fe$_3$O$_4$(111) while the oxygen-terminated FeO(111) remains adsorbate-free.[75,76]

Further oxidation for 20 min. of this film changes the film morphology drastically (Figure 14d). The satellite LEED pattern of the FeO(111) film vanishes and instead the well-known
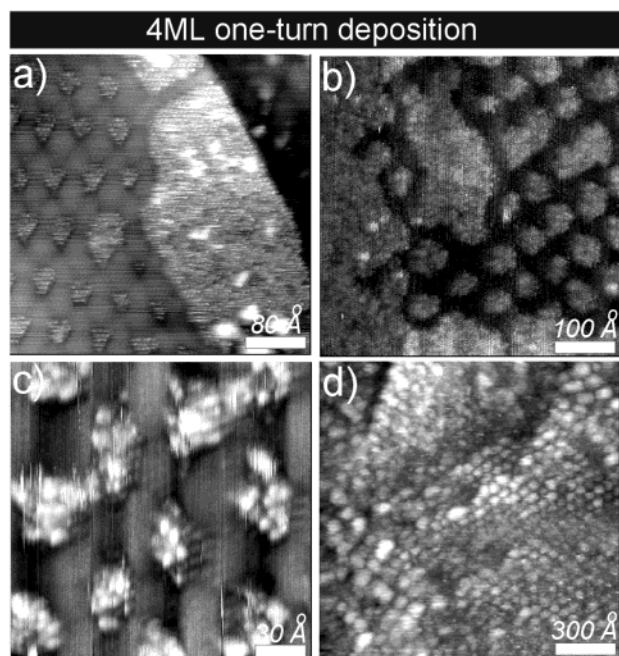
Heteroepitaxial Growth of Iron Oxide Films on Ru

J. Phys. Chem. B, Vol. 107, No. 18, 2003 **4327**

Figure 14. (a) 400×400 Å^2 STM image ($I_t = 0.3$ nA, $U_B = +0.7$ V) of $\sim$4 ML FeO(111). Fe$_3$O$_4$(111) nanostructures have periodically nucleated in the FeO(111) matrix. (b) 500×500 Å^2 STM image ($I_t = 0.7$ nA, $U_B = +0.9$ V) and (c) 180×180 Å^2 STM image ($I_t = 0.3$ nA, $U_B = +0.9$ V) after several hours in the residual gas atmosphere. Fe$_3$O$_4$-(111) domains get covered by adsorbates while FeO(111) regions remain adsorbate-free. (d) 1500×1500 Å^2 STM image ($I_t = 0.65$ nA, $U_B = +0.6$ V) after oxidation for 20 min.

pattern of pure Fe$_3$O$_4$(111) with the unexpanded lattice constant of 6 Å appears.[77] The Ru(0001)−(1 × 1) pattern but no (2 × 2) overlayer spots can be seen showing that the film is very thin but closed. STM images show cluster-like features with diameters between 30 and 100 Å (Figure 14d). Sometimes these seem to be arranged in a hexagonal periodic manner (e.g., right side of Figure 14d) which fits the pseudohexagonal arrangement of the Fe$_3$O$_4$(111)/FeO(111)nano-domain phase from where it emerged. Both STM and LEED show that the film has transformed completely into the thermodynamically more stable Fe$_3$O$_4$(111) phase upon prolonged annealing.

4. Discussion

Although a detailed picture of the growth mechanism of metals[15] and semiconductors[78] at an atomic scale has evolved, not much is known about the heteroepitaxial growth of metal oxides. At equilibrium, the heteroepitaxial growth mode depends on the surface free energies of the substrate γ_s and the film γ_f and on the interfacial energy $\gamma_{i,n}$.[79] The interfacial energy contains the so-called zero-strain contribution depending on the specific chemical interaction between film and substrate atoms. It is almost independent of the film thickness as it rapidly approaches zero with increasing distance from the interface. For $\gamma_{i,n} < 0$, atoms of the film dissolve in the substrate material under formation of an alloy phase.[80] When a material grows pseudomorphically with nonzero misfit, the interfacial energy $\gamma_{i,n}$ also contains the elastic energy which increases linearly with film thickness (number of layers n). This contribution is often the cause of a thickness-dependent change in the growth mode (Stranski-Krastanov growth). In addition, the surface free energy of ionic materials contains an electrostatic contribution (Madelung term $\gamma_{M,n}$) which may depend on the film thickness. This may lead to different growth modes which are governed

by the overall energy gain according to the equation

$$\Delta\gamma_n = \gamma_f + \gamma_{i,n} + \gamma_{M,n} - \gamma_s$$

A strict layer-by-layer growth occurs for $\Delta\gamma_n < 0$ for all n (Frank−van der Merwe mode), three-dimensional growth occurs for $\Delta\gamma_n > 0$ for all n (Volmer−Weber mode). The case in which a limited number of layers n grow in a layer-by-layer mode before three-dimensional growth starts is called Stranski-Krastanov mode. Stable islands are formed when they are larger than the critical cluster size. Dislocated islands without strain are obtained when the large activation energy for the formation of dislocations at the interface can be overcome.[78] For high deposition rates or low temperatures, a high supersaturation may be obtained from which continuously multilayers are formed since the nucleation rate of three-dimensional islands becomes very large, resulting in a pseudo Frank−van der Merwe growth.[79] The limited mobility of atoms in this case leads to preferential nucleation at those sites where the atoms are deposited while at higher temperatures or low deposition rates the diffusion lengths are larger than the terrace widths leading to step-flow growth modes.[81] In general, nucleation at steps or kinks leads to a higher contact area of the film with the substrate, so that the interface energy (when kink and step energies are neglected) becomes more important, resulting in a preferential nucleation on terraces for $\gamma_{i,n} > \gamma_s + \gamma_f$ while for $\gamma_{i,n} < \gamma_s + \gamma_f$ nucleation occurs preferentially at step edges.[35] In our experiments, it is difficult to adapt the term deposition rate to the growth of iron oxides as it is a two-step process; nevertheless, a high (low) deposition rate would correspond to a high (low) deposition rate of iron plus a short (long) oxidation time.

Generally, values for the surface free energies are either calculated or measured at high temperatures. Unfortunately, for many compounds and adsorbed phases the surface and interfacial free energies are not available.

4.1. Interaction of O$_2$ with Ru(0001). Since Ru(0001) has a high affinity toward oxygen, potential ruthenium−oxygen phases of a clean Ru(0001) surface upon the oxidation treatment used in the iron oxide growth have to be identified first. Figure 15a and b show the LEED pattern and an STM image of a Ru(0001) terrace of a submonolayer FeO(111) film after exposure to an oxygen pressure of 10^{-6} mbar for 5 min. The bright protrusions in the STM image originate from dissociated, single oxygen atoms for O coverages below 0.25 ML.[82] On some parts they have agglomerated and chains or small islands with the (2 × 2) lattice constant are formed which give rise to the weak superstructure spots in the LEED pattern. Both images confirm the formation of the well-known O/Ru(0001)−(2 × 2) phase from chemisorbed oxygen.[82−84] Even upon prolonged oxidation at this pressure, neither LEED nor STM indicate that ruthenium oxides have formed. Epitaxial RuO$_2$(110) can be obtained on Ru(0001), but the preparation of this oxide requires high oxygen pressures ($\sim$10^{-2} mbar).[23,85,86] Typical exposures in such experiments are 6×10^6 Langmuirs. Thermodynamic calculations with EQUITHERM[87] similar to those described in ref 19 reveal stability ranges of Ru and RuO$_2$ (shown in Figure 15c). The oxidation conditions in our experiments (870 K/ 10^{-6} mbar O$_2$, flash to 1000 K) are close to the phase boundary between both phases. So, thermodynamically the chemical potential of 10^{-6} mbar oxygen may be sufficient for this phase transition, nevertheless, oxidation times would amount to more than 1200 h in order to dose 6×10^6 Langmuirs. Therefore, the formation of ruthenium oxides can be ruled out and we solely observed chemisorbed oxygen species in our experiments.
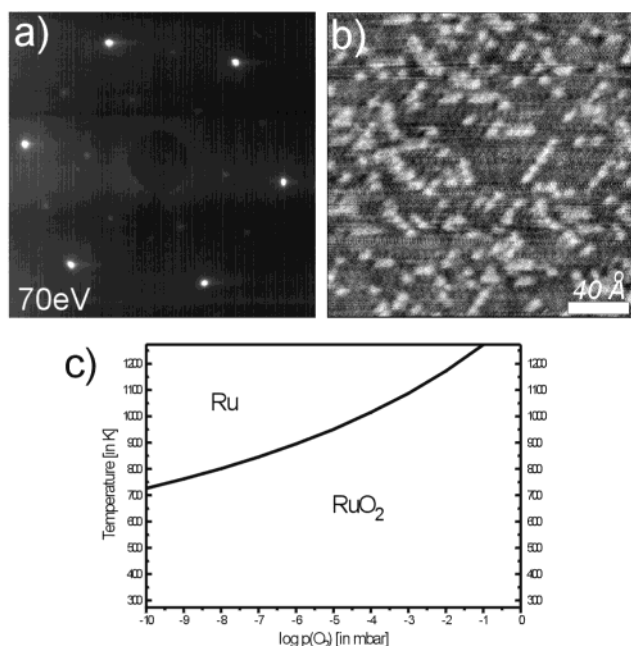
Figure 15. (a) LEED image (70 eV) and 200×200 Å^2 STM image ($I_t = 0.7$ nA, $U_B = +1.0$ V) of an uncovered Ru(0001) terrace after a typical oxidation treatment used in our experiments (10^{-6} mbar O$_2$/870 K/5 min).

4.2. Interaction of Fe with Ru(0001). The growth mechanism of Fe on Ru(0001) is not unambiguously solved in the literature. Some authors report a layer-by-layer growth (Frank−Van der Merwe)[73] while others propose a Stranski−Krastanov growth mode.[88] Kolaczkiewicz and Bauer performed experiments at different temperatures and found a layer-by-layer growth mode at room temperature, while heating between 300 and 800 K leads to an agglomeration.[89] Heating beyond 800 K leads to a spreading of the Fe due to interfacial alloying. This does not agree with our STM results which indicate that similar to the situation on Pt(111), Fe deposited at room temperature forms clusters, while at an elevated temperature of 600 K, extended Fe layers are observed. However, no strict layer-by-layer growth is observed in our experiments as second Fe layers are formed before the first Fe layer is closed. Egeberg et al. resolved the ambiguities of the growth mode by combined ion-scattering spectroscopy (ISS) and XPS experiments.[69] They found that although layers of Fe grow, the surface is never totally covered by Fe. Our STM results substantiate this proposition. For γ-Fe, a slightly smaller surface free energy (2.15 J/m^2)[90] was measured than for Ru (2.93 J/m^2),[91] which would also support a layer-by-layer growth mode for γ-Fe on Ru(0001).

Two different LEED patterns have been previously reported for Fe deposited on Ru(0001).[69,73,88,89] All authors agree that the first Fe layer on Ru(0001) grows pseudomorphically as fcc(111) with the (1×1) periodicity of the Ru(0001) substrate. Egawa et al. reported a $6\sqrt{3} \times 6\sqrt{3}R30°$ pattern after deposition of >1 ML Fe at 420 K[73] which is also found by Egeberg et al. at 500 K.[69] It was attributed to a bcc Fe(110) structure. This LEED pattern has similarities to the LEED pattern from FeO-(111) films but the Moiré periodicity is larger (∼28 Å) and the Fe atom lines are rotated by 30°. Both papers do not show the original LEED pattern, therefore it is difficult to compare it to our data. A different LEED pattern was reported by Tian et al.[88] and Kolaczkiewicz and Bauer[89] and it was attributed to an epitaxial bcc Fe(110)//Ru(0001) in 3×2 equivalent domains. This pattern is weak at room temperature but gets sharper upon annealing. Beyond 800 K, interfacial alloying occurs for films

with a thickness >4 ML.[89] Our LEED pattern corresponds to the c(4×2) oxygen phase on Fe/Ru(0001) preannealed to 1030 K as shown by Egawa et al.[72] Occasionally we observed the same LEED pattern during sputter−heating cycles. The occurrence of this LEED pattern is always accompanied by weak O−Auger intensities, therefore two prerequisites are necessary to form this phase: (1) annealing at high temperatures where interfacial alloying between Fe and Ru may occur and (2) adsorption or oxidation by oxygen which is present in the residual gas or which segregates from the Ru-substrate.

On Ru(0001), the deposited amount of Fe agrees reasonably with the Fe coverage in large scale STM images, therefore we can conclude that only limited alloying occurs at 600 K. We do not observe a LEED pattern from RuFe alloys.[89] Nevertheless, as the ruthenium substrate morphology has changed considerably after deposition of Fe at 600 K (Figure 2b), it is likely that ruthenium atoms have been replaced by iron atoms. According to LEED-IV measurements, not more than a maximum concentration of 25% Fe may form in the topmost Ru(0001) layer.[88] Previous experiments of Fe grown on Ru(0001) showed that alloying occurs for temperatures beyond 800 K.[89] The authors suggested that less-filled 3d orbitals have a stronger tendency for interfacial alloying which is believed to mediate wetting. As the oxidation in our experiments is performed at 870 K, alloying of Fe with the Ru(0001) substrate cannot be ruled out.

We can conclude that (limited) interfacial alloying might occur between Fe and Ru at elevated temperatures and very likely is more pronounced than for Fe/Pt(111). However, when RuFe alloys are oxidized at elevated temperatures, phase separation into iron oxides and metallic Ru may occur as will be discussed in the next section.

4.3. Interaction of Fe and O with Ru(0001) and Pt(111). Both iron and oxygen have a higher affinity to Ru than to Pt. The phase diagram for the binary system Fe−Pt shows various alloy phases.[92,93] Such data are rare for the Fe−Ru system and make a comparison of the interaction of Fe with a Pt vs a Ru substrate difficult. A Mössbauer comparison of bimetallic Fe−Pt and Fe−Ru catalysts supported on carbon showed that after exposing the reduced catalyst to air, the Fe−Pt/C catalyst revealed much more iron oxide and very little alloy formation while the Fe−Ru/C catalyst contained a significant amount of alloy.[94] This suggests that the interaction of Fe with Ru is stronger than with Pt, and Fe films should be higher dispersed on Ru(0001) than on Pt(111)[47] which is also evident from our experiments (compare Figure 2b with ref 47).

The interaction of bulk materials can be estimated from thermodynamic quantities such as the Gibbs free energy of formation. The Gibbs free energies of formation at 1000 K of RuO$_2$, PtO$_2$, and FeO are −245.7 kJ/mol,[20,95] −160.4 kJ/mol,[95] and −197.2 kJ/mol,[19] respectively. These data suggest that FeO/Pt should form with Fe/Pt oxidation while RuO$_2$/Fe should form from Ru/Fe after oxidation. However, FeO is not the most stable iron oxide at 1000 K which is either Fe$_3$O$_4$ (−264.0 kJ/mol) or α-Fe$_2$O$_3$ (−280.4 kJ/mol) (depending on the oxygen pressure).[19] Therefore, also on Ru, the oxidation of iron is favored over the formation of RuO$_2$. The formation of FeO benefits from low oxygen partial pressures as the formation of 1 mol of FeO requires only 1/2 mol of O$_2$ while the formation of RuO$_2$ and PtO$_2$ require 1mol of O$_2$.[19] As discussed in Section 4.1, we never observed RuO$_2$ in our experiments.

The interaction of oxygen with the specific surface orientations of Pt and Ru can be estimated from thermal desorption spectroscopy (TDS) experiments. The activation energy for

Heteroepitaxial Growth of Iron Oxide Films on Ru

J. Phys. Chem. B, Vol. 107, No. 18, 2003 **4329**

desorption of oxygen from Pt(111) amounts to 55−30 kcal/mol.[96−98] Oxygen desorption from Ru(0001) requires higher activation energies of 90−80 kcal/mol.[99]

Growth of Al_2O_3 films on a Ru(0001) substrate showed that upon heating at high temperatures (∼1000 K) an AlRu interface alloy is formed while heating at low temperatures in oxygen oxidizes Ru atoms in the interface region.[100] However, in these experiments much higher oxygen exposures were used (up to 2×10^5 L). The growth of Cu films on an O-precovered Ru(0001) surface showed that preadsorbed oxygen atoms act as a surfactant, i.e., they are displaced from the Ru surface and transported to the top of the growing Cu film under formation of an oxidized Cu layer with Cu at the interface.[101−103] Keeping in mind that Fe is much less noble than Cu, the same stacking sequence might occur for FeO(111) films on Ru(0001). Such oxygen-terminated FeO(111) bilayers have been found on Pt(111) and Pt(100) which are bound via an iron layer to the Pt substrate.[104−106] Also the structural similarity with the LEED pattern from Fe films on Ru(0001) by Egawa et al. suggests a similar interface coincidence structure as discussed above.[73] During sputter−annealing cycles we found that AES-clean Ru(0001) samples produce an FeO(111) LEED pattern with significant Fe Auger intensities upon annealing in oxygen, thus we can conclude that dissolved Fe segregates to the substrate surface and phase separation into FeO and Ru occurs upon oxidation.

In summary, we assume the same stacking sequence to be present in FeO(111) films on Ru(0001) and on Pt(111). However, we cannot rule out that interfacial alloying or an oxygen termination at the interface has formed. As STM images of FeO(111) on both substrates are very similar, at least the same oxygen termination seems very likely. Electron-scattering quantum chemistry calculations of the image contrast in STM images for FeO(111) films with Pt tips came to the conclusion that the protrusions correspond to oxygen atoms.[105] If we follow this explanation, the atomic defects seen in Figure 11g are oxygen vacancies. Such defects were not observed for FeO(111) films on Pt(111) and would not be expected for bulk FeO as it is a cation-deficient structure.[107] However, as long as the stacking sequence is not unambiguously structurally characterized, the true nature of these defects remains speculative as they may also be due to an electronic effect in STM imaging.

4.4. Initial Iron Oxide Growth. Similar as on Pt(111), iron oxides start to grow as FeO(111) bilayers which are laterally expanded compared to bulk FeO. In both cases, growth is not pseudomorphic and specific coincidence structures are formed at the interface to the substrate. For the surface free energies of FeO, Ru, and Pt, values of 0.6 J/m,[2,108] 2.93 J/m,[2,91] and 2.34 J/m,[2,109] respectively, have been reported. Although a monolayer FeO(111) film does not represent FeO bulk material, these values support the observed wetting behavior and a layer-by-layer growth mode for FeO(111) films on Ru(0001) which from the surface free energies is even more favored than on Pt(111).

According to the classification introduced by Tasker,[110] FeO(111) films are polar and should not be stable since each iron−oxygen bilayer produces an electric dipole field which increases the surface potential of the oxide film (see Figure 16). This results in a thickness-dependent electrostatic Madelung contribution to the surface energy $\gamma_{M,n}$ that increases with the number of layers n. Nevertheless, polar films can be stabilized up to a certain thickness by large relaxations which reduce the electrostatic FeO(111) surface dipole.[49] The critical thickness up to which FeO(111) films form on Ru(0001) is 4 ML and thus is larger than on Pt(111) where a maximum of 2.5 ML
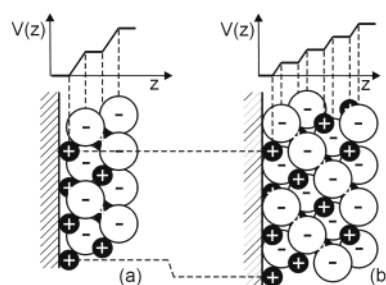

Figure 16. Layer structure of FeO(111) on Ru and dipole-induced surface potential. (a) For 2 ML, slightly relaxed "7 on 8" FeO(111) coincidence structure (O−O distance 3.08 Å). (b) For 4 ML, strongly relaxed "6 on 8" FeO(111) coincidence structure (O−O distance 3.58 Å).

was observed. Even when thicker films (3 ML) are deposited on Pt(111) and oxidized for only 1min, no thicker FeO(111) films are obtained but multilayer growth of $Fe_3O_4(111)$ occurs.[48]

The reason for this different behavior on both substrates is a combination of several effects. The higher surface free energy of Ru, the higher affinity of Ru to both Fe and O, and the Madelung energy gain due to the expansion of the lattice constant in the third and fourth FeO layer. The first FeO(111) monolayer interacts more strongly with the Ru substrate than with a Pt substrate and thus is perfectly aligned with the Ru(0001) substrate which was not observed on Pt(111). This strong interaction of Fe and O with Ru proceeds in the second FeO(111) monolayer which aligns with the underlying first monolayer and thus is also perfectly aligned with the substrate. In the third and fourth monolayer, the lattice constant is expanded to 3.58 Å forming the "6 on 8" structure while the perfect alignment of the FeO(111) film to the substrate is maintained. On Pt(111), FeO(111) is not always perfectly aligned with the substrate and it forms also rotated coincidence structures with a maximum lattice constant expansion to 3.4 Å.[49] The FeO(111) film "floats" on the Pt(111) while on Ru(0001), the strong interaction at the interface makes it more favorable to align the films with the substrate by locking 7 or even 6 FeO units in place of 8 Ru atoms, even if this requires a tremendous expansion of the lattice constant. This lattice constant expansion on one hand reduces the electrostatic dipole as will be discussed in the next paragraph and on the other hand enables an inward relaxation of the Fe−O interlayer distances which brings the first oxygen layer closer to the Ru substrate (see Figure 16) which might also be more favorable on Ru than on Pt due to the higher affinity of Ru to oxygen. (Note that a similar situation occurs for an oxygen termination at the interface as in this case the iron layer comes closer to the Ru substrate which is also stabilizing).

The lattice expansion when going from the "7 on 8" FeO(111) structure on the second layer to the "6 on 8" coincidence structure on the third monolayer can only be understood if a relaxation perpendicular to the surface is assumed so that the layer distances may be reduced from 1.25 Å (bulk value) to about 0.6 Å when assuming constant Fe−O bond distances. The dipole potential per bilayer is reduced correspondingly, and the surface potential of 4 ML of the "6 on 8" coincidence structure equals approximately that of 2 ML of the "7 on 8" coincidence structure (see Figure 16)[64] The electrostatic energy gain due to this lattice expansion even compensates the associated changes in the interfacial and surface free energy of the film which arise from the large deviation from the FeO bulk lattice constant. Thus, in ionic films where bonds are not strongly directed, the strongest contribution to stabilize such polar films comes from

the minimization of the Madelung energy while strain effects resulting from bond bending are of minor importance. This is in contrast to previous observations in the field of metal-oxide heteroepitaxy where the growing oxide exhibited a remarkable stiffness which led to the formation of misfit dislocations or a film buckling by formation of mosaic grains.[14,111] However, this is not a contradiction, as the examples where the oxides appear as stiff materials all are nonpolar films such as MgO(100), and thus no energy gain due to a reduction of the dipole moment by relaxations or lattice constant changes is possible. Covalent contributions are neglected in this view but may additionally stabilize the film as already slight changes of the covalent vs ionic character enables a significant reduction of the Madelung energy. The formation of $Fe_3O_4(111)$ nanodomains in 4 ML thick FeO(111) films further reduces the average Madelung energy since $Fe_3O_4(111)$ is terminated by 1/4 ML Fe cations.[77] $Fe_3O_4(111)$ domains form at crossing points of dark lines in the FeO(111) Moiré pattern. For FeO films on Pt(111), dark areas correspond to topographically higher regions[105] and if this applies to Ru, too, these are areas where the destabilizing polar oxygen termination rises up representing locally the most instable regions.

4.5. $Fe_3O_4(111)$ Island Formation. FeO is not thermodynamically stable at our preparation conditions[19] and these films represent a metastable phase which is initially stabilized by the interaction with the Ru substrate. Thermodynamically, Fe_3O_4 should form at these conditions. In fact, when Fe is deposited and oxidized sequentially in submonolayer steps, the FeO(111) layer grows only up to about 1.5 ML. Further deposition leads to the formation of $Fe_3O_4(111)$ islands and thus a Stranski-Krastanov growth mode similar to the growth on Pt(111). Different from growth on Pt(111), $Fe_3O_4(111)$ islands on Ru, once formed, grow by oxidizing the surrounding FeO(111) monolayer film and "eating it up" (see Figure 6f). In this way, the FeO(111) film is removed.

Also 2−3 ML thick FeO(111) films transform into the thermodynamically more stable $Fe_3O_4(111)$ phase. Initially, these films wet the substrate. Upon prolonged annealing, nucleation of $Fe_3O_4(111)$ islands takes place. The nucleation is not homogeneous and occurs preferentially at step edges (Figures 9a, 10). Once these islands have formed, they also grow at the expense of the surrounding FeO(111) film which is removed in this way.

We have previously suggested that the formation of $Fe_3O_4(111)$ requires a minimum iron oxide amount larger than one monolayer.[64] One reason could be that the repeat unit along the [111] direction is 4.85 Å and comprises two oxygen layers, separated by inequivalent iron layers (mix-trigonal and kagomé, see Figure 1b). In bulk Fe_3O_4, even three such repeat units in ABC packing represent the periodicity along [111] (14.55 Å), and therefore the height of Fe_3O_4 islands is often at least in the range of 20 Å.

On the 4 ML thick FeO film, spontaneous formation of ordered Fe_3O_4 domains was observed. This is not only due to the thickness of the film but to the fact that 4 ML FeO allow a stoichiometric transformation into 5 layers Fe_3O_4 with correct surface termination by simple oxidation (see Figure 17): The occupation of Fe-sublayers in $Fe_3O_4(111)$ is only 3/4 compared to FeO and keeping the Fe amount constant, exactly five Fe layers plus 1/4 layer as surface termination[77] can be produced from four full Fe layers in FeO under oxidative conditions. A stoichiometric conversion is not possible for FeO(111) films with a thickness below 4 ML without creating a defective Fe_3O_4-(111) film or local height variations. It seems therefore likely, that a minimum thickness of 4 ML FeO is necessary to form
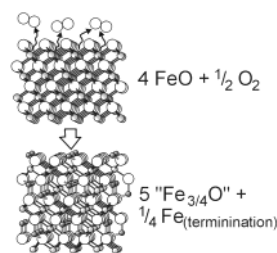

Figure 17. Schematic representation showing the conversion of a 4 ML thick FeO(111) film to $Fe_3O_4(111)$. $Fe_3O_4(111)$ films are terminated by 1/4 ML Fe cations and for one stoichiometric $Fe_3O_4(111)$ repeat unit plus 1/4 ML Fe-termination exactly 4 ML FeO(111) are necessary.

Fe_3O_4. For thinner films, this thickness may locally be reached most easily at steps where Fe atoms from the upper terrace may diffuse with a certain probability to the lower terrace at oxidation temperatures beyond 870 K. Once an $Fe_3O_4(111)$ island has nucleated, the surrounding FeO(111) film accumulates more easily at the island side facets. Diffusion limitations have also been discussed to be responsible for the temperature-dependent initial thickness of FeO(111) films grown on Pt(111) before $Fe_3O_4(111)$ islands are formed (870 K: 2.5 ML FeO(111); 1000 K: 1 ML FeO(111)).[47] The formation of $Fe_3O_4(111)$ islands on Pt(111) with a height of at least 20 Å is accelerated at 1000 K due to the higher mobility of iron oxide.

The ∼4 ML thick FeO(111) films transform completely to $Fe_3O_4(111)$, but in this case, the nucleation mechanism is homogeneous and no influence of substrate defects on the island formation is observed. A supersaturated solution of iron or of an oxide precursor is generated from which self-assembled, periodic $Fe_3O_4(111)$ domains nucleate in the FeO(111) film. Upon prolonged oxidation, this inverse biphase ordered structure transforms completely to $Fe_3O_4(111)$ clusters and finally to a closed $Fe_3O_4(111)$ film. This shows that the superstructure of $Fe_3O_4(111)/FeO(111)$ shown in Figure 14a−c is only metastable representing the initial nucleation stage of the thermodynamically favored phase transition to $Fe_3O_4(111)$.[19]

For the thinner FeO(111) films, the required thickness of 4 ML is most easily achieved near step edges where iron oxide diffusion from an upper terrace to an adjacent FeO film could locally establish the required thickness. For a low interface energy, nucleation is expected to be more likely at step edges ($\gamma_{i,n} < \gamma_s + \gamma_f$, see discussion above). Due to the discussed strong interaction of Ru with both Fe and O, it is very likely that this condition is fulfilled. On Pt(111), where the interaction of both atoms is considerably weaker, no influence of steps on the nucleation of Fe_3O_4 islands was observed.[47]

As FeO(111) films are not stable once $Fe_3O_4(111)$ has formed, we assume that no FeO(111) film persists below $Fe_3O_4(111)$ islands and thus $Fe_3O_4(111)$ islands directly grow on the Ru(0001) substrate with its bulk lattice constant. The high mismatch of the oxygen sublattice in $Fe_3O_4(111)$ (2.97 Å) with the Ru(0001) substrate (2.70 Å) may result in a high interfacial energy $\gamma_{i,n}$ so that a Volmer−Weber growth mode occurs for $Fe_3O_4(111)$ on Ru(0001) despite the low surface free energy of Fe_3O_4 (0.4 J/m²). As the interfacial energy $\gamma_{i,n}$ increases with film thickness, the island character of $Fe_3O_4(111)$ is more pronounced in thicker films. Thus the homogeneous nucleation in 4 ML thick FeO(111) films leads preferentially to extended hexagonal crystallites while the local, iron oxide diffusion-controlled heterogeneous nucleation yields well-defined trigonal or hexagonal islands.

The different growth scenarios of iron oxide films depending on the initial FeO(111) thickness are summarized in Figures
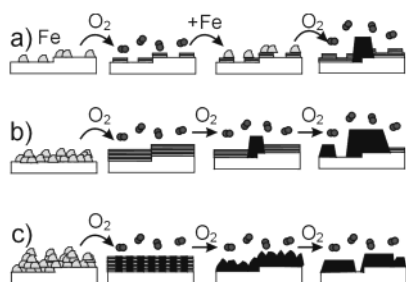
Heteroepitaxial Growth of Iron Oxide Films on Ru

J. Phys. Chem. B, Vol. 107, No. 18, 2003 **4331**

Figure 18. Schematic representation of different growth scenarios of iron oxides on Ru(0001). (a) Deposition of submonolayer amounts of iron and subsequent oxidation yields a pseudo Stranski−Krastanov growth mode. (b) Deposition of 1−3 ML thick FeO(111) and subsequent oxidation yields thick FeO(111) films which transform upon prolonged oxidation into Fe_3O_4(111) islands nucleating at step edges. (c) Deposition of ∼4 ML Fe and subsequent oxidation leads to the nucleation of self-assembled, periodic Fe_3O_4(111) in a thick FeO(111) film which transform completely to Fe_3O_4(111) upon prolonged oxidation.
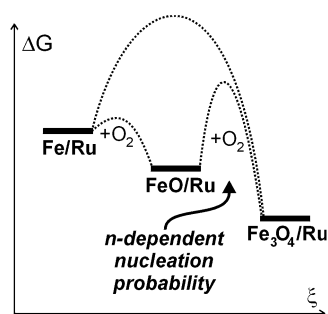

Figure 19. Schematic energy diagram for the two-step oxidation of Fe to Fe_3O_4. Metastable FeO(111) films can be obtained because the activation energy for the phase transition to the thermodynamically more stable Fe_3O_4(111) is high and nucleation depends on the FeO(111) film thickness as a critical thickness of 4 ML has to be established by diffusion processes.

18 and 19. The thermodynamic stability increases in the order Fe < FeO < Fe_3O_4.[19] The activation energy for the formation of FeO(111) can be overcome at 870 K and metastable FeO(111) films are formed. We assume that the activation energy for the transformation of FeO(111) to Fe_3O_4(111) is larger and that the nucleation probability depends on the FeO-(111) film thickness. The phase transition to Fe_3O_4(111) is faster the thicker the FeO(111) film is. Thick polar FeO(111) layers can no longer be stabilized and the system tries to gain energy by transforming into the more stable Fe_3O_4(111). The system adopts a compromise for each Fe amount, oxidation time, and temperature. The high number of parameters results in the reported wealth of structures. As the observed film structures strongly depend on the oxidation kinetics, all intermediates and mixtures of wetting FeO(111) films, inverse biphase ordered FeO(111)/Fe_3O_4(111) nanostructures, extended Fe_3O_4(111) crystallites, and well-defined hexagonal Fe_3O_4(111) islands can be obtained.

Interface-stabilized oxide structures have also been found for vanadium oxides on Pd(111).[54] There, at least 3 monolayer equivalents oxide coverage (or 4.5 V_2O_3 layers) are required to form a stable V_2O_3(0001) bulk phase. As pointed out by these authors, metastable, interface-mediated oxide phases may occur generally in the early stages of oxide growth and bulk oxide structures are of little relevance.

4.6. Self-Assembly of Fe_3O_4(111) Nanostructures. Periodically arranged self-assembled nanostructures often form on strained, prepatterned substrate systems, e.g., on strained Cu

films on Ru(0001)[42] or by deposition of Ag islands on 2 ML thick Ag films on Pt(111).[41] In our experiments, we used the Moiré pattern of thin FeO(111) films where Fe_3O_4(111) nanodomains nucleate at locally most unstable electrostatic positions. Similar to the Cu relaxation structures on Ru(0001) by Günther et al., the formation of these structures crucially depends on the thickness of the film, nevertheless, the driving force is electrostatics and thermodynamics rather than strain relaxation. Such self-assembled periodic domain structures have been theoretically predicted by Vanderbilt for two materials with different work functions.[112]

The observed nanostructures might be interesting for applications in magnetic devices. The size makes them potential candidates for the use in quantum magnetic disks[43] where the Fe_3O_4(111) nanodomains could act as one-particle-per-bit magnetic units embedded in a nonmagnetic FeO(111) film. However, the small size of the nanodomains raises doubt whether these domains are beyond the superparamagnetic limit. Magnetic measurements with a spin-polarized STM as has been performed on Fe_3O_4(001)[113] might give insight in this point.

5. Conclusions

We have used scanning tunneling microscopy (STM) and low-energy electron diffraction (LEED) for heteroepitaxial growth studies of iron oxides on Ru(0001). Initially, FeO(111) layers wet the substrate and grow in a Frank−Van der Merwe growth mode. Up to 4 monolayers FeO(111) can be grown on Ru(0001). Polar FeO(111) films are metastable and transform to Fe_3O_4(111) which is thermodynamically and electrostatically more stable for the conditions used in our experiments. Two different nucleation mechanisms for Fe_3O_4(111) occur depending on the FeO(111) film thickness. On FeO(111) films with a thickness between 1 and 3 ML a heterogeneous nucleation of Fe_3O_4(111) islands starts at step edges. Homogeneous nucleation of self-assembled, periodic Fe_3O_4(111) nanodomains embedded in an ultrathin FeO(111)−Moiré occurs in ∼4ML thick FeO(111) films. FeO(111) films completely transform to Fe_3O_4(111) upon prolonged oxidation. The overall growth mode is controlled by oxidation kinetics. Growth of iron oxides on Ru(0001) is different than on Pt(111) where not more than 2.5 ML FeO(111) are obtained before island growth of Fe_3O_4(111) starts (Stranski−Krastanov growth). These results show that the growth of metal oxides is quite complex and determined by several contributions (surface free energies, interfacial energy, electrostatics, thermodynamics of phase transitions, kinetics). Therefore, the stabilization mechanism and growth mode for the same metal oxide phases depends strongly on the substrate.

As our results are mainly based on morphological surface structure changes imaged by STM and qualitative LEED images, quantitative structural information would be of help in order to verify the presented hypotheses of the discussed structural evolution of film structures, particularly at the several monolayer level.

References and Notes

(1) Gunter, P. L. J.; Niemantsverdriet, J. W.; Ribeiro, F. H.; Somorjai, G. A. *Catal. Rev.−Sci. Eng.* **1997**, *39*, 77.

(2) Street, S. C.; Xu, C.; Goodman, D. W. *Annu. Rev. Phys. Chem.* **1997**, *48*, 43.

(3) Campbell, C. T. *Surf. Sci. Rep.* **1997**, *27*, 1.

(4) Freund, H.-J. *Angew. Chem.* **1997**, *109*, 444.

(5) Henry, C. R. *Surf. Sci. Rep.* **1998**, *31*, 235.

(6) Bäumer, M.; Freund, H.-J. *Prog. Surf. Sci.* **1999**, *61*, 127.

(7) Peden, C. H. F.; Herman, G. S.; Ismagilov, I. Z.; Kay, B. D.; Henderson, M. A.; Kim, Y.-J.; Chambers, S. A. *Catal. Today* **1999**, *51*, 513.

(8) Weiss, W.; Schlögl, R. *Top. Catal.* **2000**, *13*, 75.

(9) Chusuei, C. C.; Lai, X.; Luo, K.; Goodman, D. W. *Top. Catal.* **2001**, *14*, 71.

(10) Henrich, V. E.; Cox, P. A. *The Surface Science of Metal Oxides*; Cambridge University Press: Cambridge, 1994.

(11) Noguera, C. *Physics and Chemistry at Oxide Surfaces*; Cambridge University Press: Cambridge, 1996.

(12) Wang, X.-G.; Weiss, W.; Shaikhutdinov, Sh. K.; Ritter, M.; Petersen, M.; Wagner, F.; Schlögl, R.; Scheffler, M. *Phys. Rev. Lett.* **1998**, *81*, 1038.

(13) Noguera, C. *J. Phys.: Condens. Matter* **2000**, *12*, R367.

(14) Chambers, S. A. *Surf. Sci. Rep.* **2000**, *39*, 105.

(15) Pacchioni, G. *Surf. Rev. Lett.* **2000**, *7*, 277.

(16) Wang, X.-G.; Chaka, A.; Scheffler, M. *Phys. Rev. Lett.* **2000**, *84,* 3650.

(17) Freund, H.-J.; Kuhlenbeck, H.; Libuda, J.; Rupprechter, G.; Bäumer, M.; Hamann, H. *Top. Catal.* **2001**, *15*, 201.

(18) Ketteler, G.; Weiss, W.; Ranke, W. *Surf. Rev. Lett.* **2001**, *8*, 661.

(19) Ketteler, G.; Weiss, W.; Ranke, W.; Schlögl, R. *Phys. Chem. Chem. Phys.* **2001**, *3,* 1114.

(20) Reuter, K.; Scheffler, M. *Phys. Rev.* **2002**, *B65*, 035406.

(21) Ranke, W.; Weiss, W. *Prog. Surf. Sci.* **2002**, *70,* 1.

(22) Stampfl, C.; Ganduglia Pirovano, M. V.; Reuter, K.; Scheffler, M. *Surf. Sci.* **2002**, *500*, 368.

(23) Over, H.; Kim, Y. D.; Seitsonen, A. P.; Wendt, S.; Lundgren, E.; Schmid, M.; Varga, P.; Morgante, A.; Ertl, G. *Science* **2000**, *287*, 1474.

(24) Freund H.-J.; Kuhlenbeck, H.; Staemmler, V. *Rep. Prog. Phys.* **1996**, *59*, 283.

(25) Hannemann, H.; Ventrice, C. A.; Bertrams, Th.; Brodde, A.; Neddermeyer, H. *Phys. Status Solidi* **1994**, *146*, 289.

(26) Voogt, F. C.; Hibma, T.; Zhang, G. L.; Hoefman, M.; Niesen, L. *Surf. Sci.* **1995**, *331*, 1508.

(27) Batzill, M.; Beck, D. E.; Koel, B. E. *Phys. Rev.* **2001**, *B64*, 245402.

(28) Lind, D. M.; Berry, S. D.; Chern, G.; Mathias, H.; Testardi, L. R. *Phys. Rev.* **1992**, *B45*, 1838.

(29) Gao, Y.; Kim, Y. J.; Chambers, S. A. *J. Vac. Sci. Technol. A* **1997**, *15*, 332.

(30) Boffa, A. B.; Galloway, H. C.; Jacobs, P. W.; Benitez, J. J.; Batteas, J. D.; Salmeron, M.; Bell A. T.; Somorjai, G. A. *Surf. Sci.* **1995**, *326*, 80.

(31) Zhang, L.; Kuhn, M.; Diebold, U. *Surf. Sci.* **1997**, *375*, 1.

(32) Brune, H. *Surf. Sci. Rep.* **1998**, *31*, 121.

(33) Venables, J. A. *Surf. Sci.* **1994**, *299/300*, 798.

(34) Zhang, Z.; Lagally, M. G. *Science* **1997**, *276*, 377.

(35) Bauer, E. Z. *Kristallogr.* **1958**, *110*, 372 and 395.

(36) Shchukin, V. A.; Bimberg, D. *Rev. Mod. Phys.* **1999**, *71*, 1125.

(37) Nötzel, R.; Temmyo, J.; Tammamura, T. *Nature* **1994**, *369*, 131.

(38) Tersoff, J.; Teichert, C.; Lagally, M. G. *Phys. Rev. Lett.* **1996**, *76*, 1675.

(39) Teichert, C. *Phys. Rep.* **2002**, *365*, 335.

(40) Chambliss, D. D.; Wilson, R. J.; Chiang, S. *Phys. Rev. Lett.* **1991**, *66*, 1721.

(41) Brune, H.; Gionannini, M.; Bromann, K.; Kern, K. *Nature* **1998**, *394*, 451.

(42) Günther, C.; Vrijmoeth, J.; Hwang, R. Q.; Behm, R. J. *Phys. Rev. Lett.* **1995**, *74*, 754.

(43) Chou, S. Y.; Krauss, P. R.; Kong, L. *J. Appl. Phys.* **1996**, *79*, 6101.

(44) Sorenson, T. A.; Morton, S. A.; Waddill, G. D.; Switzer, J. A. *J. Am. Chem. Soc.* **2002**, *124*, 7604.

(45) Bäumer, M.; Libuda, J.; Freund, H.-J. In *Chemisorption and Reactivity on Supported Clusters and Thin Films*; Lambert, R. M., Pacchioni, G., Eds.; Kluwer Academic Press: NATO ASI Series E, 1997; pp 61−104.

(46) Chambers, S. A.; Droubay, T.; Jennison, D. R.; Mattson, T. R. *Science* **2002**, *297*, 827.

(47) Weiss, W.; Ritter, M. *Phys. Rev.* **1999**, *B59*, 5201.

(48) Kim, Y. J.; Westphal, C.; Ynznza, R. X.; Wang, Z.; Galloway, H. C.; Salmeron, M.; Van Hove, M. A.; Fadley, C. S. *Surf. Sci.* **1998**, *416*, 68.

(49) Ranke, W.; Ritter, M.; Weiss, W. *Phys. Rev.* **1999**, *B60*, 1527.

(50) Ritter, M.; Ranke W.; Weiss, W. *Phys. Rev.* **1998**, *B57*, 7240.

(51) Shaikhutdinov, Sh.; Ritter, M.; Weiss, W. *Phys. Rev.* **2000**, *B62*, 7535.

(52) Koveshnikov, A. N.; Madjoe, R. H.; Karunamuni, J.; Stockbauer, R. L.; Kurtz; R. J. *J. Appl. Phys.* **2000**, *87*, 5929.

(53) Gota, S.; Guiot, E.; Henriot, M.; Gautier-Soyer, M. *Surf. Sci.* **2000**, *454−456*, 796.

(54) Surnev, S.; Kresse, G.; Ramsey, M. G.; Netzer, F. P. *Phys. Rev. Lett.* **2001**, *87*, 086102.

(55) Surnev, S.; Vitali, L.; Ramsey, M. G.; Netzer, F. P.; Kresse, G.; Hafner, J. *Phys. Rev.* **2000**, *B61*, 13945.

(56) Surnev, S.; Kresse, G.; Sock, M.; Ramsey, M. G.; Netzer, F. P. *Surf. Sci.* **2001**, *495*, 91.

(57) Fujii, T.; Takano, M.; Katano, R.; Bando Y.; Isozumi, Y. *J. Appl. Phys.* **1989**, *66*, 3168.

(58) Geus, J. W. *Appl. Catal.* **1986**, *25*, 313.

(59) Muhler, M.; Schlögl R.; Ertl, G. *J. Catal.* **1992**, *138*, 413.

(60) Kuhrs, C.; Arita, Y.; Weiss, W.; Ranke, W.; Schlögl, R. *Top. Catal.* **2001**, *14*, 111.

(61) Condon, N. G.; Leibsle, F. M.; Lennie, A. R.; Murray, P. W.; Vaughan D. J.; Thornton, G. *Phys. Rev. Lett.* **1995**, *75*, 1961.

(62) Condon, N. G.; Leibsle, F. M.; Parker, T.; Lennie, A. R.; Vaughan D. J.; Thornton, G. *Phys. Rev.* **1997**, *B55*, 15885.

(63) Shaikhutdinov, Sh. K.; Ritter, M.; Wang, X.-G.; Over, H.; Weiss, W. *Phys. Rev.* **1999**, *B60*, 11062.

(64) Ketteler, G.; Ranke, W. *Phys. Rev.* **2002**, *B66*, 033405.

(65) Sanchez, J. P.; Ravet, M. F.; Piecuch, M.; Maurer, M. *Hyperfine Interact.* **1990**, *57*, 2077.

(66) Liu, C.; Bader, S. D. *Phys. Rev.* **1990**, *B41*, 553.

(67) Berry, F. J.; Liwu, L.; Chengyu, W.; Renyuan, T.; Su, Z.; Dongbai, L. *J. Chem. Soc., Faraday Trans. 1* **1985**, *81*, 2293.

(68) Urabe, K.; Ozaki, A. *J. Catal.* **1978**, *52*, 542.

(69) Egeberg, R. C.; Dahl, S.; Logadottir, A.; Larsen, J. H.; Norskov, J. K.; Chorkendorff, I. *Surf. Sci.* **2001**, *491*, 183.

(70) Weiss, W.; Ritter, M.; Zscherpel, D.; Swoboda, M.; Schlögl, R. *J. Vac. Sci. Technol.* **1998**, *A16*, 21.

(71) Gsell, M.; Jakob, P.; Menzel, D. *Science* **1998**, *280*, 717.

(72) Egawa, C.; Sawabe, K.; Iwasawa, Y. *J. Chem. Soc., Faraday Trans. 1* **1988**, *84*, 321.

(73) Egawa, C.; Aruga, T.; Iwasawa, Y. *Surf. Sci.* **1987**, *188*, 563.

(74) Shaikhutdinov, Sh.; Weiss, W. *J. Mol. Catal. A: Chem.* **2000**, *158*, 129.

(75) Joseph, Y.; Kuhrs, C.; Ranke, W.; Ritter, M.; Weiss, W. *Chem. Phys. Lett.* **1999**, *314*, 195.

(76) Joseph, Y.; Ranke, W.; Weiss, W. *J. Chem. Phys.* **2000**, *B104*, 3224.

(77) Ritter M.; Weiss, W. *Surf. Sci.* **1999**, *432*, 81.

(78) Pehlke, E.; Moll, N.; Kley, A.; Scheffler, M. *Appl. Phys.* **1997**, *A65*, 525.

(79) Bauer E.; van der Merve, J. H. *Phys. Rev.* **1986**, *B33*, 3657.

(80) Tersoff, J. *Phys. Rev. Lett.* **1995**, *74*, 434.

(81) Himpsel, F. J.; Ortega, J. E.; Mankey, G. J.; Willis, R. F. *Adv. Phys.* **1998**, *47*, 511.

(82) Wintterlin, J.; Trost, J.; Renisch, S.; Schuster, R.; Zambelli, T.; Ertl, G. *Surf. Sci.* **1997**, *394,* 159.

(83) Meinel, K.; Wolter, H.; Ammer, Ch.; Beckmann, A.; Neddermeyer, H. *J. Phys.: Condens. Matter* **1997**, *9*, 4611.

(84) Madey, T. E.; Engelhardt, H. A.; Menzel, D. *Surf. Sci.* **1975**, *48*, 304.

(85) Kim, Y. D.; Seitsonen, A. P.; Wendt, S.; Wang, J.; Fan, C.; Jacobi, K.; Over, H.; Ertl, G. *J. Phys. Chem.* **2001**, *B105*, 3752.

(86) Reuter, K.; Scheffler, M. *Phys. Rev.* **2002**, *B65,* 035406.

(87) Equitherm. *Database and software package for chemical equilibrium calculations on personal computers,* Version 3.02; VCH Scientific software: New York, 1993.

(88) Tian, D.; Li, H.; Jona, F.; Marcus, P. M. *Solid State Commun.* **1991**, *80*, 783.

(89) Kolaczkiewicz, J.; Bauer, E. *Surf. Sci.* **1999**, *423*, 292.

(90) Price A. T.; Holl, A. H.; Greenough, A. P. *Acta Met.* **1964**, *12*, 49.

(91) Gasteiger, H. A.; Ross, P. N.; Cairns, E. J. *Surf. Sci.* **1993**, *293*, 67.

(92) Hultgren, R.; Desai, P. D.; Hawkins, D. T.; Gleiser, M.; Kelley, K. K.; Wagman, D. D. *Selected values of the thermodynamic properties of binary alloys*; American Society for Metals: Metals Park, OH, 1973.

(93) Cabri, L. J.; Feather, C. E. *Can. Mineral.* **1975**, *13*, 117.

(94) Guerrero-Ruiz, A.; Sepulveda-Escribano, A.; Rodriguez-Ramos, I. *Appl. Catal. A: Gen.* **1992**, *81*, 81.

(95) *CRC Handbook of Chemistry and Physics*, 76th ed.; CRC Press: Boca Raton, FL, 1995.

(96) Campbell, C. T.; Ertl, G.; Kuipers, H.; Segner, J. *Surf. Sci.* **1981**, *107*, 207.

(97) Parker, D. H.; Bartram, M. E.; Koel; B. E. *Surf. Sci.* **1989**, *217*, 489.

(98) Zhdanov, V. P.; Kasemo, B. *Surf. Sci.* **1998**, *415*, 403.

(99) Madey, T. E.; Engelhardt, H. A.; Menzel, D. *Surf. Sci.* **1975**, *48*, 304.

(100) Wu, Y.; Tao, H.-S.; Madey, T. E.; Shinn, N. D. *Surf. Sci.* **1995**, *336*, 123.

(101) Kalki, K.; Schick, M.; Ceballos, G.; Wandelt, K. *Thin Solid Films* **1993**, *228*, 36.

(102) Ammer, C.; Meinel, K.; Beckmann, A.; Neddermeyer, H.; Heinz, K. *Surf. Sci.* **2001**, *482−485*, 1298.

Heteroepitaxial Growth of Iron Oxide Films on Ru

J. Phys. Chem. B, Vol. 107, No. 18, 2003 **4333**

(103) Schmidt, M.; Wolter, H.; Wandelt, K. *Surf. Sci.* **1994**, *307−309*, 507.

(104) Fadley, C. S.; Van Hove, M. A.; Hussain Z.; Kaduwela, A. P. *J. Electron Spectrosc.* **1995**, *75*, 273.

(105) Galloway, H. C.; Sautet, P.; Salmeron, M. *Phys. Rev.* **1996**, *B54*, R11145.

(106) Shaikhutdinov, Sh. K.; Ritter, M.; Weiss, W. *Phys. Rev.* **2000**, *B62*, 7535.

(107) Cornell, R. M.; Schwertmann, U. *The Iron Oxides*; VCH: Weinheim, 1996.

(108) Overbury, S. H.; Bertrand, P. A.; Somorjai, G. A. *Chem. Rev.* **1975**, *75*, 547.

(109) Blakely, J. M.; Mykura, H. *Acta Met.* **1962**, *10*, 565.

(110) Tasker, P. W. *J. Phys. C: Solid State Phys.* **1979**, *12,* 4977.

(111) Wollschläger, J.; Erdos, D.; Schroder, K. M. *Surf. Sci.* **1998**, *402−404*, 272.

(112) Vanderbilt, D. *Surf. Sci. Lett.* **1992**, *268*, L300.

(113) Wiesendanger, R.; Shvets, I. V.; Bürgler, D.; Tarrach, G.; Güntherodt, H.-J.; Coey, J. M. D. *Science* **1992**, *255*, 583.